Establishing a *D*-Band Waveguide Impedance Standard Including the Random Effects of a Vector Network Analyzer for 6G Wireless Communications

Chihyun Cho (조치현), *Senior Member, IEEE*, Tae-Weon Kang (강태원), *Senior Member, IEEE*, Jae-Yong Kwon (권재용), *Senior Member, IEEE*, and Hyunji Koo (구현지), *Member, IEEE*

***Abstract*— This article describes an established *D*-band waveguide impedance standard. The eight-term vector network analyzer (VNA) error model is used for our measurement system. A set of shims, a flush short, thru, and a reciprocal device are used as calibration standards to determine the error coefficients of the VNA error model. From the measured raw scattering parameters and dimensions of each shim, the error coefficients of the error model, the propagation constant of the shim, and the reflection coefficient of the flush short are found using nonlinear optimization. Then, we evaluate the uncertainty in the scattering parameter measurement by combining the fitting uncertainty, the dimension uncertainty of the shims, and the random effects of the VNA into the residual uncertainty model. Finally, we calculate the calibration and measurement capabilities (CMCs) of our measurement system.**

***Index Terms*— Impedance, measurement standards, measurement uncertainty, residual model, sub-terahertz (sub-THz), waveguide.**

I. Introduction

VARIOUS studies are currently being conducted to support the development of 6G communications. 6G communication is intended to achieve speeds of 10 Gbps, latency within 0.1 ms, and coverage of 10 km, requiring more than a bandwidth of 10 GHz [1], [2]. Accordingly, the millimeter-wave (mm-wave) band and the sub-Terahertz (sub-THz) band are being discussed as candidate frequencies for 6G communication [3]. The sub-THz band is more attractive than the mm-wave band since the sub-THz band can continuously use a bandwidth of several tens of gigahertz, while the mm-wave band has already been allocated for other purposes.

In the metrological area, studies have been conducted on establishing traceability of waveguide impedance in the mm-wave and sub-THz bands [4], [5], [6], [7], [8], [9]. However, only a few national metrology institutes (NMIs) have registered sub-THz band impedances as calibration and measurement capabilities (CMCs) on the International Bureau of Weights and Measures (BIPM). In [10] and [11], we briefly introduced a scattering parameter (S-parameter) measurement method with traceability in the *D*-band and presented the evaluated random effects of a vector network analyzer (VNA). Unlike previous studies, instead of using the thru-reflect-line (TRL) algorithm, we applied a nonlinear optimization algorithm, similar to [12]. This made it possible to calculate the uncertainty of the optimization parameters from the fitting residuals. In addition, it can use multiple shims and reciprocal adapters as calibration standards to improve measurement results without any discontinuity from 110 to 170 GHz. This also allows for the rigorous estimation of uncertainty, similar to [6] and [13], including the random effects of the VNA. In the sub-THz band, a different evaluation method than the guidelines in [14] is required. We propose a new technique to evaluate the measurement system's drift, nonlinearity, and test port cable stability.

The reflections and transmissions of electromagnetic (EM) waves in a linear network are described by the S-parameters, and usually, a VNA is used to measure them. The fundamental concept and the procedure for establishing impedance standards are described extensively in [15]. The reference plane for the S-parameter measurements is defined at the end of the test port adapters, waveguide, or coaxial connector, to which calibration standards and a device under test (DUT) are connected. The eight-term VNA error model is used to correct the systematic error. The error coefficients consisting of the error model are determined from the raw S-parameters of the calibration standards using known properties. The properties of the calibration standards are modeled using conductivity and dimensions traceable to SI units. The measured raw S-parameters of the DUT are corrected with the error coefficient determined through calibration using the

Manuscript received 24 January 2023; revised 7 May 2023; accepted 14 June 2023. Date of publication 3 July 2023; date of current version 14 July 2023. This work was supported by the Physical Metrology for National Strategic Needs funded by the Korea Research Institute of Standards and Science under Grant KRISS-2022-GP2022-0002. The Associate Editor coordinating the review process was Dr. Ari Feldman. *(Corresponding author: Tae-Weon Kang.)*

Chihyun Cho, Tae-Weon Kang, and Hyunji Koo are with Electromagnetic Wave Metrology Group, Korea Research Institute of Standards and Science, Daejeon 34113, South Korea (e-mail: chihyun.cho@kriss.re.kr; twkang@kriss.re.kr; hyunji.koo@kriss.re.kr).

Jae-Yong Kwon is with Electromagnetic Wave Metrology Group, Korea Research Institute of Standards and Science, Daejeon 34113, South Korea, and also with the Department of Science of Measurement, University of Science and Technology, Daejeon 34113, South Korea (e-mail: jykwon@kriss.re.kr).

Digital Object Identifier 10.1109/TIM.2023.3291794

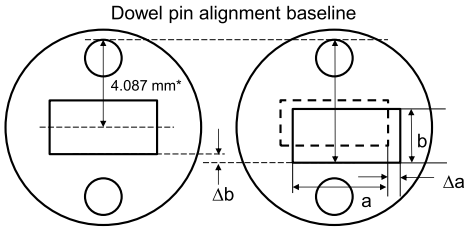

Fig. 1. Waveguide dimensions (4.087 mm for D-band is from IEEE 1785.2-2016). a and b are the width and height of the waveguide aperture, and Δa and Δb are the deviations of the aperture center of a shim under test from the aperture's assigned center, the midpoint of a line segment connecting the centers of the two dowel pin holes. Note the dowel pin alignment baseline is perpendicular to the line segment during geometry measurement.

calibration standard. As a result, the error coefficient's uncertainty determines the DUT measurement's uncertainty. The uncertainty of the DUT also depends on the random effects of the VNA, including auxiliary devices such as waveguide frequency extenders. Therefore, to evaluate the measurement uncertainty, we need to include the random effects of the VNA error model.

The remaining parts of this article are as follows. Section II discusses the dimension measurement and modeling of a waveguide calibration standard, i.e., shims. In Section III, the eight-term VNA error model is described and the S-parameter modeling of waveguide calibration standards is detailed. Section IV describes the measurement system and techniques for enhancing system stability. Section V explains the measurement uncertainty evaluated using the residual model. The random effects of the VNA are evaluated in Section VI and the CMC management is explained in Section VII. Concluding remarks follow in Section VIII.

II. Shims and Their Modeling

In this work, shims, a flush short, thru, and a reciprocal device are used as calibration standards. Among those standards, the S-parameters of the shims are modeled here and numerically validated. For this, the dimensions of each shim are measured and the S-parameters of the shims are calculated.

A. Dimension Measurements

The dimensions of the shims are measured using a vision system that is calibrated using a calibration chart on which reference patterns have been printed in various sizes from 0.02 to 4 mm. The dimensions of each pattern of the calibration chart are calibrated from the Length Group of the Korea Research Institute of Standards and Science (KRISS). The measured dimension of the shims and the expanded uncertainty ($k = 2$) are summarized in Table I. The uncertainty contributions are the uncertainty of the calibration chart, manufacturer's specifications, and repeated measurements. In sub-THz measurement, a dowel pin is highly recommended [8]. Thus, all dimensions are measured using the upper tangential line of the dowel pin as a reference line (see Fig. 1). a and b represent the width and height of the shim. Δa and Δb indicate the offset values, and l is the length of the shim.

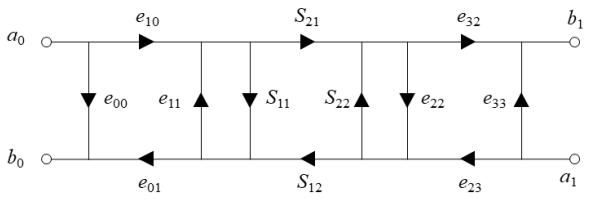

Fig. 2. Eight-term VNA error model. S_{11}, S_{21}, S_{12}, and S_{22} are the S-parameters of the DUT. e_{00}, e_{11}, and $e_{10}e_{01}$ are directivity, port-1 match, and reflection tracking, respectively. e_{33}, e_{22}, and $e_{32}e_{23}$ are directivity, port-2 match, and reflection tracking, respectively.

B. Modeling of Shim

Based on the measured dimensions, we calculate the S-parameters of the shim using the closed-form formula [16] and compare it to the commercial 3-D EM software, HFSS, for validation. In the comparison, the reflection S_{11} shows a negligibly small difference in both magnitude and phase, while transmission S_{21} shows a slight difference in magnitude. However, this small difference is not crucial since the propagation constant γ of the shims is found in the calibration process.

The reason for using the closed-form formula, not the commercial 3-D EM software, is to calculate the S-parameter uncertainty due to the uncertainty of the dimension measurement. In HFSS, a fine mesh is required to obtain high accuracy in the finite element method (FEM) analysis, and it usually takes more than 15 min per structure. Thus, to calculate the sensitivity for the dimensions, 15 min per parameter is required. But if we use the closed-form formula, we can significantly reduce time while maintaining accuracy.

III. VNA Error Model

The eight-term VNA error model used is shown in Fig. 2. We determine the error coefficient of the VNA error model using the measured raw S-parameters of shims, thru, a flush short, and a reciprocal device. To convert the raw measurements based on the switched source to an eight-term error model, we need to correct the switch error term in the measured value [17], [18]. Since the scattering coefficient is the relative ratio, e_{10} can be normalized to 1. The total cascaded scattering matrix is

$$S_{\text{DUT,meas}} = \begin{bmatrix} e_{00} & e_{01} \\ e_{10} & e_{11} \end{bmatrix} \oplus \begin{bmatrix} S_{11} & S_{12} \\ S_{21} & S_{22} \end{bmatrix} \oplus \begin{bmatrix} e_{22} & e_{23} \\ e_{32} & e_{33} \end{bmatrix} \tag{1}$$

where $\oplus$ represents the cascade of the S-parameters [19]. Since the cascade of the S-parameters is complex, it can be represented as simple form T-parameters, i.e., a transmission ($ABCD$) matrix

$$T_{\text{DUT,meas}} = X T_{\text{DUT}} Y. \tag{2}$$

The T-parameters of DUT can be obtained by de-embedding each port error box, X and Y, from the measured value. Thus, it is necessary to find the error coefficients of the eight-term error model so that the de-embedding value of $X^{-1}T_{\text{DUT,meas}}Y^{-1}$ approaches to that of T_{DUT} as close as possible within a specified tolerance. Usually, this is a nonlinear

optimization problem. In this article, the error coefficients of the eight terms, the conductivity σ_{shim} of the shims, and the reflection coefficients Γ_{refl} of the reflection standard were found by nonlinear least squares optimization using the "lsqnonlin" function of MATLAB, as follows:

$$f(G) = \sum |y_{\text{def}} - y_{\text{fit}}(x)|^2, \quad (x = e_{00}, e_{11}, \ldots, \sigma_{\text{shim}}, \Gamma_{\text{refl}}). \tag{3}$$

This becomes a problem to find the x that minimizes $f(G)$. Here, y_{fit} and y_{def} are as follows:

$$y_{\text{fit}} = X^{-1} T_{\text{REF,meas}} Y^{-1} \tag{4}$$

$$y_{\text{def}} = \text{TP}_X^{-1} T_{\text{REF}} \text{TP}_Y^{-1}. \tag{5}$$

TP_X^{-1} and TP_Y^{-1} represent the T-parameters converted from the S-parameters generated by misalignment and dimensions of the test ports, port-1 and port-2, respectively [16], [20].

The S-parameters corresponding to the T-parameters of calibration standards T_{REF} in (5) are as follows. Note that the S-parameters and T-parameters are readily convertible to each other.

First, the scattering coefficient of the thru is, by definition, as follows:

$$S_{\text{Thru}} = \begin{bmatrix} 0 & 1 \\ 1 & 0 \end{bmatrix}. \tag{6}$$

Second, the scattering coefficient of the shim can be calculated from the measured dimensions as described in Section II-B. Although the conductivity of the shim is unknown, it is assumed that all shims have the same loss. The surface roughness of the walls on the shims causes additional loss. Accurate surface roughness measurement is possible using laser scanning [21]. The vision system we used is difficult to measure the surface roughness. Thus, we model the conductivity σ_{shim}, including the effect of surface roughness, as follows [15], and the values of σ_{DC} and σ_{HF} are determined in the calibration process:

$$\sigma_{\text{shim}} = \sigma_{\text{DC}} - \sqrt{\frac{f}{1\ \text{GHz}}}\sigma_{\text{HF}}. \tag{7}$$

Then the attenuation constant α_{10} and the phase constant $\beta_{10}$for the TE_{10} mode are as follows:

$$\alpha_{10} = \frac{R_m}{ab\beta_{10}k_0 z_0}\left(2bk_{c,10}^2 + ak_0^2\right) \tag{8}$$

$$\beta_{10} = \sqrt{k_0^2 - k_{c,10}^2} \tag{9}$$

where the wavenumber in free space k_0, the cutoff wavenumber for the TE_{10} mode $k_{c,10}$, the surface resistance for the waveguide wall R_m, and the characteristic impedance of free space z_0 are as follows, with $\omega = 2\pi f$ (f is frequency in Hz), the permeability μ_0, and the permittivity ε_0 in free space [22]:

$$k_0 = \omega\sqrt{\mu_0\varepsilon_0} \tag{10}$$

$$k_{c,10} = \pi/a \tag{11}$$

$$R_m = \sqrt{\frac{\omega\mu_0}{2\sigma_{\text{shim}}}} \tag{12}$$

$$z_0 = \sqrt{\frac{\mu_0}{\varepsilon_0}}. \tag{13}$$

TABLE I
MEASURED DIMENSIONS OF SHIMS AND EXPANDED UNCERTAINTIES IN mm

	SN: 300002	SN: 279832	SN: 279831
a	1.6550 ± 0.00139	1.6491 ± 0.00159	1.6552 ± 0.00168
b	0.8303 ± 0.00136	0.8244 ± 0.00293	0.8309 ± 0.00171
Δa	0 ± 0.00137	0.0004 ± 0.00136	0.0002 ± 0.00135
Δb	0.0159 ± 0.00147	0.0063 ± 0.00258	0.0144 ± 0.00184
l	0.8206 ± 0.00305	1.9065 ± 0.00258	2.8100 ± 0.00273

Therefore, the scattering coefficient of the ith shim is

$$S_{\text{shim},i} = \begin{bmatrix} S_{11,i} & e^{-\gamma l_i} \\ e^{-\gamma l_i} & S_{22,i} \end{bmatrix} \tag{14}$$

with the propagation constant

$$\gamma = \alpha_{10} + j\beta_{10} \tag{15}$$

where α_{10} and β_{10} are given by (8) and (9), respectively. Note that all shims have the same propagation constant γ. Here, $S_{11,i}$ and $S_{22,i}$ are the reflections caused by the shim aperture size (a, b) and the misalignment, and l_i represents the length of each shim.

Third, it is assumed that the scattering coefficients of the reflection standards measured at both ports are the same

$$S_{\text{refl}} = \begin{bmatrix} \Gamma_{\text{refl}} & 0 \\ 0 & \Gamma_{\text{refl}} \end{bmatrix}. \tag{16}$$

In this article, we apply the flush short as the reflection standard, and the impedance z_{refl} and the reflection coefficient Γ_{refl} are modeled as [15]

$$z_{\text{refl}} = z_1 + \sqrt{\frac{f}{1\ \text{GHz}}}z_2 + \frac{f}{1\ \text{GHz}}z_3 \tag{17}$$

$$\Gamma_{\text{refl}} = \frac{z_{\text{refl}} - z_o}{z_{\text{refl}} + z_o}. \tag{18}$$

Finally, a reciprocal device is used as a calibration standard. In this way, the transmission coefficient after calibration is optimized so that $S_{\text{recip},S_{21}} = S_{\text{recip},S_{12}}$.

If there are many variables in the optimization, the result may reach the local minimum depending on the initial value. In this study, to solve this problem, we find the initial value of the error coefficients, the conductivity σ of the shim, and Γ_{refl} of the reflection standard found from the multiline TRL method [23].

IV. MEASUREMENT SYSTEM

Fig. 3 shows the overall configuration of the impedance measurement system. A VNA and frequency extender(s) are used to measure the S-parameters. We also designed and installed an alignment system, cooling system, and cable support fixture for precise measurement.

A. Alignments

The higher the frequency, the shorter the wavelength, so aligning the measurement system is essential to obtain good raw data. A frequency extender is usually required to measure signals above 67 GHz using a commercial VNA.

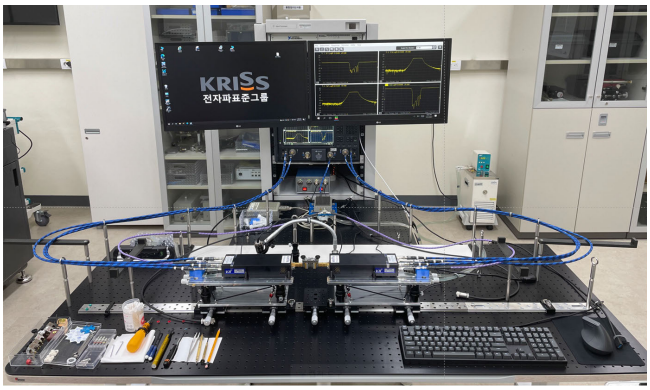

Fig. 3. Photograph of the measurement system.

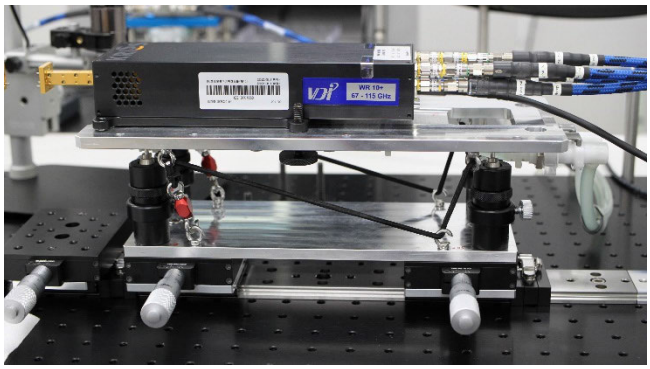

Fig. 4. Alignment system for VNA frequency extenders.

A frequency extender is a device that multiplies the VNA's signal into a target frequency band. The alignment of the frequency extender is essential because it connects directly to the DUT.

As shown in Fig. 4, we configure the frequency extender to be movable on the rail and install height adjustment terminals at each of the four places to adjust the height. In addition, to adjust the position of the plane, a stage that can move left or right was installed at the front and rear, respectively. This makes it possible to arrange the frequency extender at an arbitrary position in the 3-D space. The cable supporter keeps the cable in the same position even if the frequency extender moves to measure the DUT or shim, as shown in Fig. 3.

B. Common Local Oscillator (LO)

To operate the frequency extender, a LO and RF signals are required. In our system, the RF signals are generated at ports one and two, respectively, and LO signals are generated at ports three and four of the VNA. Suppose the LO signals on ports three and four are connected separately to each frequency extender. In that case, the automatic level loop control (ALC) circuit will operate separately for each port, resulting in a phase change during long-term measurements [6], [24]. Therefore, to prevent this, after receiving the LO signal from a single port, it is amplified and branched using a splitter and distributed to each extender. Since the power of the LO signal is insufficient (usually, a power of 10 dBm per extender is required), the LO signal is amplified using an amplifier before branching, as shown in Fig. 5(a). Fig. 5(b) and (c) represent the

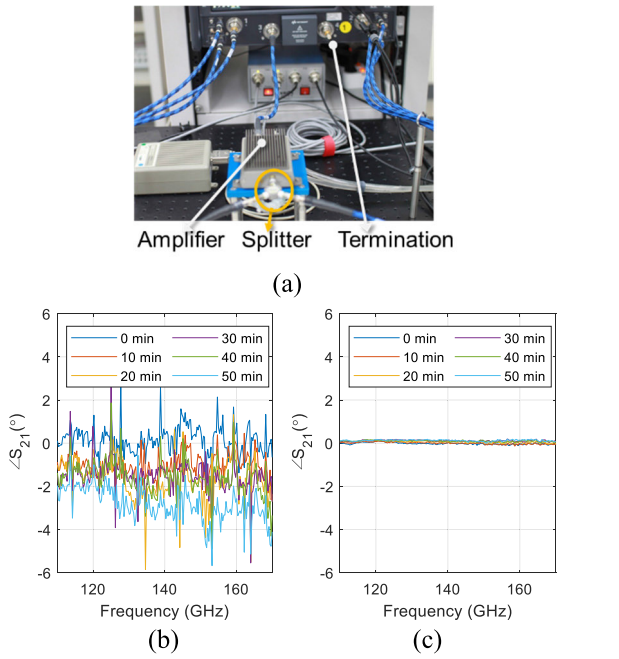

Fig. 5. Drift due to LO. (a) Common LO measurement setup. (b) S_{21} without common LO. (c) S_{21} with common LO.

Fig. 6. Cooling system for (a) frequency extenders and (b) common LOs amplifier.

difference in S_{21} depending on the time when with and without common LO. Over time, the phase is drastically changed when applying an individual LO. However, the common LO results in a phase ten times more stable than that of the individual LO.

C. Cooling System

The frequency extender is composed of non-linear active elements, so heat is inevitably generated (it usually heats up more than 30 °C). Therefore, even if the laboratory temperature is stably managed at 23 °C, thermal expansion occurs on the calibration standards or DUT, making it difficult to measure the S-parameters accurately [25].

Thus, the waveguide section on the frequency extender, which is usually connected to the DUT, should be maintained at 23 °C. In our case, we applied a cooling water system. Fig. 6 shows the setup to supply cooled water to the bottom of the stage installed by the frequency extender and the bottom of the amplifier of the LO. Fig. 7 shows the effect of the cooling system. The temperature of the waveguide sections and the chassis of the frequency extenders is reduced by about 23 °C. Next, we measured the 2-port S-parameters of the shim. Fig. 7(c) shows the measurement result. The cooling system

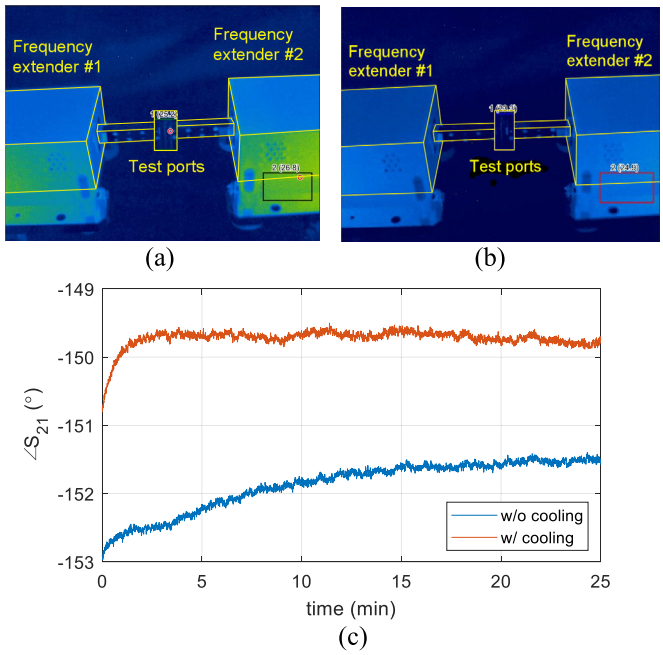

Fig. 7. Cooling effect. (a) Temperature of the frequency extenders and test port without cooling. (b) Temperature of the frequency extenders and test port with cooling. (c) Phase variation of the shim with time.

shows a faster saturation result on measuring the phase of the transmission coefficients S_{21} and S_{12}. Note that the amplitude of all S-parameters did not change critically. It may be that the temperature variation due to the RF source has more effect on the length of the shim, not the aperture size. Anyway, the cooling system used can significantly reduce the temperature saturation time.

D. Connecting the Waveguide

Bolts are usually used to connect the two waveguide flanges. However, this can take a long time, even for experienced users, due to its small size and space. To solve this problem, we employ a waveguide connection clamp [6], [26]. Fig. 8 shows a comparison of the bolt and the clamp, respectively. The repeatability is the standard deviation of ten measurements. The result shows that their repeatability is almost identical. Accordingly, we apply the clamp, which immensely helps to reduce the connection time.

V. Uncertainty Analysis

We can evaluate the uncertainty of the error coefficients found in the optimization by applying a calculation method for the uncertainty of parameters in a nonlinear regression [27]

$$\sigma_{\text{fit}}^2 = \frac{\sum |y_{\text{def}} - y_{\text{fit}}|^2}{v} \tag{19}$$

$$v = n_{\text{observ}} - n_{\text{param}} \tag{20}$$

$$\text{Cov}_{\text{fit}} = \left(J'_{GX} J_{GX}\right)^{-1} \sigma_{\text{fit}}^2. \tag{21}$$

Here, v is the value obtained by subtracting n_{param}, the number of parameters used for optimization from n_{observ}, and the number of observation points. J_{GX} is a Jacobian matrix

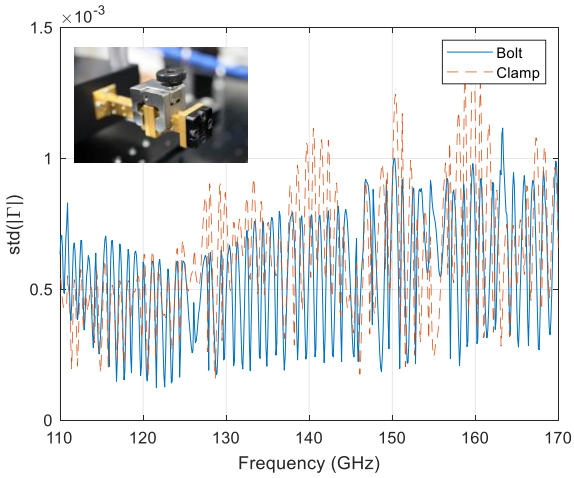

Fig. 8. Comparison of connection repeatability for bolt- and clamp-connections of waveguide flanges. The inset figure represents the connected waveguide using the clamp.

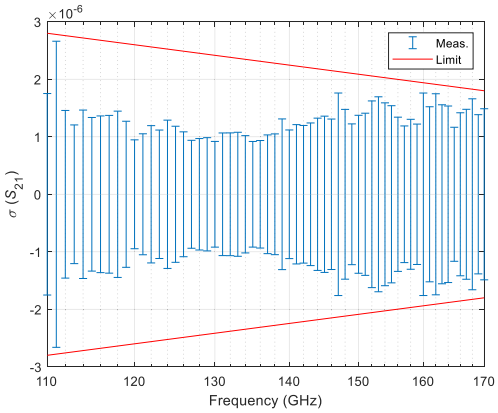

Fig. 9. Noise floor of VNA.

representing the sensitivity coefficient of $f(G)$ in (3) for the parameter x [15].

We also account for the error term's uncertainty due to the uncertainty in dimension measurement. Usually, we would perform each optimization per dimension change on their dimensional uncertainty. Since this approach is time-consuming, the National Institute of Standards and Technology (NIST, USA) and the Federal Institute of Metrology (METAS, Switzerland) suggest novel approaches [15], [28]. NIST determines the error terms and changes the value of the DUT according to the dimensions. Then the error terms are again combined to create a new measured value. After that, calibration is repeated to perform calculations, including dimensional uncertainty. In METAS, the chain rule propagates dimensional uncertainty to error term uncertainty. In this article, we used the METAS approach

$$J_{XP} = \left(J'_{GX} J_{GX}\right)^{-1} J'_{GX} J_{GP} \tag{22}$$

$$\text{Cov}_{\text{dim}} = J_{XP} U_{\text{dim}} J'_{XP}. \tag{23}$$

J_{XP} is a Jacobian matrix representing the sensitivity coefficient of the error terms by the dimensions, and to obtain it, the sensitivity coefficient J_{GX} of the optimization function by each error term [that is calculated in (21)] and the sensitivity

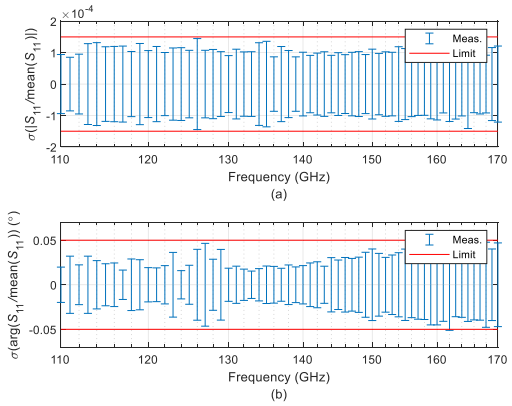

Fig. 10. Trace noise of VNA. (a) Magnitude. (b) Phase.

coefficient J_{GP} of the optimization function by dimension are obtained. Then, after calculating J_{XP} by applying the chain rule, the covariance $\mathrm{Cov}_{\mathrm{dim}}$ of the error term by dimensions is calculated, as given in (23). U_{dim} is the covariance, where the diagonal element is the square of the standard uncertainty of the shim dimension measurements and the off-diagonal elements are zeros. We now combine the two covariances to calculate the final uncertainty for the error terms

$$\mathrm{Cov}_{\text{error term}} = \mathrm{Cov}_{\mathrm{fit}} + \mathrm{Cov}_{\mathrm{dim}}. \tag{24}$$

Unlike the VNA error model, the residual model proposed in [29] and [30] assumes that the VNA is fully calibrated, and then represents the residual uncertainties generated after calibration as directivity residual (δ), source match residual (μ), and reflection tracking residual (τ), respectively. The advantage of the residual model is that the uncertainty calculation is easy, the VNA calibration values can be used as is, and raw measurements are not required. In this study, we convert the VNA error model, which was optimized using the calibration standards, into a residual model.

VI. Evaluation of the VNA

In this section, we describe how to characterize the random effects of the VNA. The random effects are modeled as noise floor (N_L), trace noise (N_H), nonlinearity (L), drift (D_{ij}), test port cable stability (CA_{ij}), and connector repeatability (CO_R), respectively. The noise floor, trace noise, and connector repeatability are evaluated using the guidelines [14]. We have proposed a novel technique to evaluate the other parts (nonlinearity, drift, and test port cable stability) in sub-THz [11]. In this article, $\Re(\cdot)$, $\Im(\cdot)$, $|\cdot|$, and $\angle$ refer to the real, imaginary, magnitude, and phase (in degree) of the argument, respectively.

A. Noise Floor and Trace Noise

We evaluate the noise floor and trace noise. First, after connecting high reflection standards (flush short in this study) to both ends of the VNA test port, we measure the 2-port S-parameters 500 times in continuous wave (CW) mode. After that, the standard deviation of S_{21} becomes the noise floor, and the standard deviation normalized to the average value of S_{11} becomes the trace noise. The measurement results are shown in Figs. 9 and 10. We set a limit that the measured value does not exceed and assign it to the noise floor and trace noise, respectively.

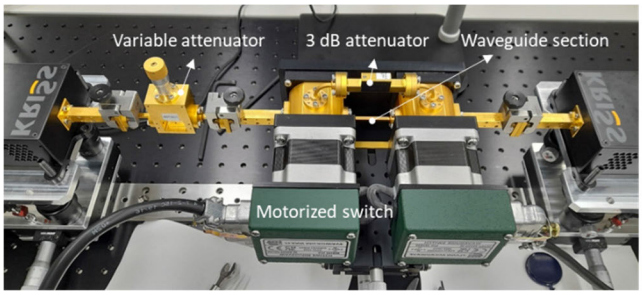

Fig. 11. Measurement setup for the nonlinearity of VNA.

B. Nonlinearity

Next, the nonlinearity of the network analyzer is evaluated. The guideline recommends using a preevaluated attenuator. However, since there is no standard for D-band attenuation yet, we use the following method.

We connect a variable attenuator and two motorized switches between the two extenders, as shown in Fig. 11. And between the two motorized switches, a 3-dB attenuator and a waveguide section are connected according to the path. Then, by operating the motorized switch, the S_{21} of the path to which the waveguide section is connected is measured. Then, by operating the motorized switch again, we select the path to which the 3 dB attenuator is connected and measure S_{21}. The difference between the two paths is then recorded. Then, we adjust the variable attenuator to attenuate by about 5 dB. Then, we measure and record the difference between the above two paths again. This is repeated until S_{21} reaches about 40 dB using a variable attenuator. Then, each difference value is compared to evaluate linearity. Fig. 12 shows the measurement results. We found that the S_{11} and S_{22} of the variable attenuator used remained almost the same below 10 dB but varied significantly between the 0 and 5 dB settings. In nonlinearity evaluation, the change in the reflection coefficient according to the power setting makes it difficult to evaluate nonlinearity accurately [31]. Therefore, we excluded the measurement results of 0 and 5 dB. The evaluated nonlinearity of the VNA is about 0.015 dB, including the repeatability of the used switch of 0.004 dB, as shown in Fig. 12.

C. Drift

For the drift evaluation, we use the motorized switch described above. Short, offset short, and load are connected to the end of each path of the motorized switch, respectively, and the S-parameters of each path are measured every 10 min for 24 h. The short and offset short deviations measured over 24 h were up to 0.012 and 0.046 dB, respectively, including switch repeatability of 0.004 dB. To calculate the drift of the residual model, the VNA is calibrated for each measurement time using the first measurement value ($t = 0$) as the definition. Therefore, $e_{00} = 0$, $e_{11} = 0$, and $e_{10}e_{01} = 1$ at $t = 0$, and the

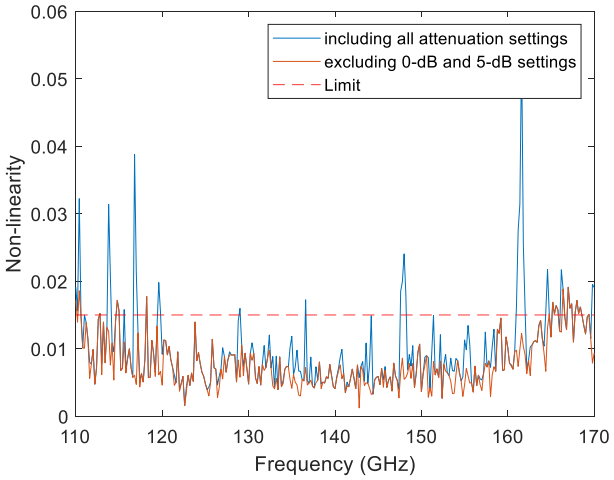

Fig. 12. Nonlinearity of VNA.

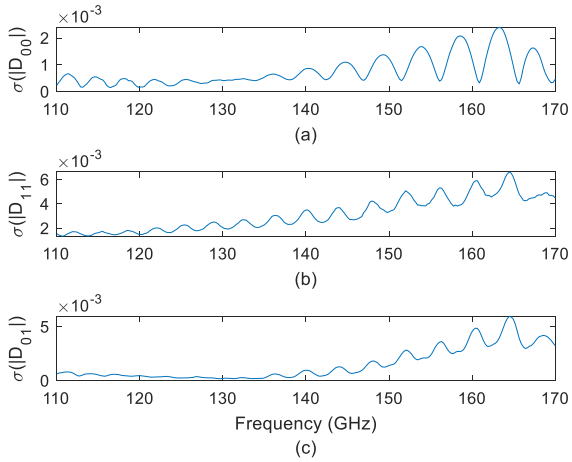

Fig. 13. Drift of VNA. (a) D_{00}. (b) D_{11}. (c) D_{01}.

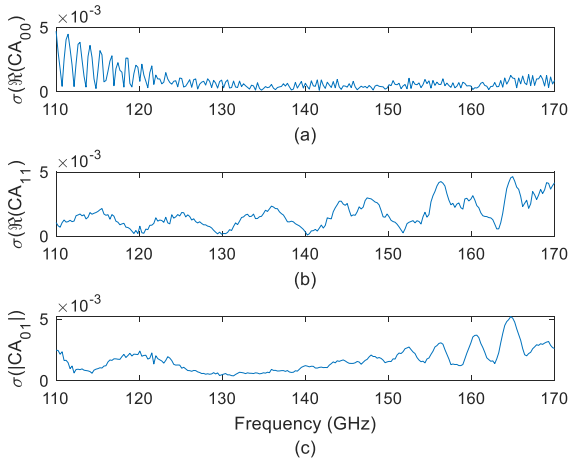

Fig. 14. Test port cable stability. (a) CA_{00}. (b) CA_{11}. (c) CA_{01}.

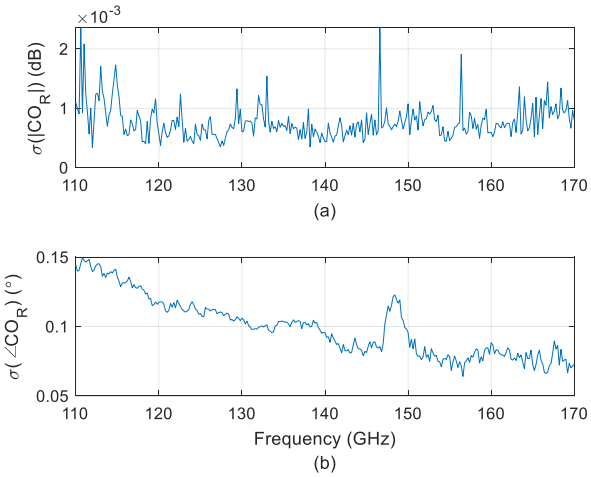

Fig. 15. Connection repeatability. (a) Magnitude. (b) Phase.

change values of each error term according to elapse time can be obtained. Fig. 13 shows drift D_{ij} measured over 24 h, which can be confirmed as low drift due to the cooling system used.

D. Test Port Cable Stability

Stability due to test port cable movement is measured using a drift measurement system. After selecting seven measurement locations on the rail, the S-parameters of the short, offset short, and load are measured at each location. Similar to the drift measurement, the first measured value is set as a definition in the one-port calibration. Then, the change amount of e_{00}, e_{11}, and $e_{10}e_{01}$ terms is determined using each measured value and assigned to CA_{ij}, as shown in Fig. 14. Unlike the coaxial impedance measurement system, the uncertainty caused by test port cable movement is not significant since the IF signal around 20 GHz is transmitted through the VNA and cable after the D-band signal is up/down-converted in the frequency extender.

E. Connection Repeatability

Finally, connection repeatability is measured by connecting a short to the test port according to the guideline [13]. The measured standard deviation is divided in half and assigned to the forward and backward directions. Measured results are shown in Fig. 15.

VII. CMC Management and Comparison

We calculate the CMC of the S-parameters in D-band using the residual model including the random effects of VNA. The measurement model combining the random effects of VNA in the previous section and the residual model recently proposed [30] is shown in Fig. 16. The scattering coefficient S_{ij} of a DUT has uncertainty due to random effects as well as residual errors of VNA. For example, Fig. 17 shows the uncertainty of the 1-port S-parameter measurement when the reflection coefficient of the DUT is 1. See the appendix for a detailed description of the uncertainty calculation. Depending on the phase of the DUT, it has different values of uncertainty. The CMC is the smallest among the uncertainty values at each frequency. Tables II and III are the CMC tables of 1-port and 2-port S-parameter measurements calculated using the above method.

Next, we measure the reflection coefficient of a power sensor and evaluate its uncertainty. For comparison, the Physikalisch-Technische Bundesanstalt (PTB) and the KRISS

TABLE II
CMC TABLES FOR 1-PORT REFLECTIONS

$\|S_{ii}\|$	Magnitude	Phase (°)
0	0.006 ~ 0.010	-
0.1	0.006 ~ 0.010	3.7 ~ 6.2
0.2	0.006 ~ 0.010	1.9 ~ 3.1
0.3	0.006 ~ 0.009	1.4 ~ 2.1
0.4	0.007 ~ 0.010	1.1 ~ 1.7
0.5	0.007 ~ 0.011	1.0 ~ 1.5
0.6	0.008 ~ 0.012	0.9 ~ 1.4
0.7	0.009 ~ 0.014	0.9 ~ 1.3
0.8	0.010 ~ 0.016	0.8 ~ 1.3
0.9	0.011 ~ 0.019	0.8 ~ 1.3
1	0.012 ~ 0.021	0.8 ~ 1.3

TABLE III
CMC TABLES FOR 2-PORT TRANSMISSIONS

$\|S_{ij}\|$ (dB)	Magnitude (dB)	Phase (°)
0	0.10 ~ 0.14	0.7 ~ 1.1
-3	0.10 ~ 0.14	0.7 ~ 1.1
-6	0.10 ~ 0.14	0.7 ~ 1.1
-10	0.10 ~ 0.14	0.7 ~ 1.1
-20	0.10 ~ 0.14	0.7 ~ 1.1
-30	0.10 ~ 0.14	0.7 ~ 1.1
-40	0.12 ~ 0.16	0.9 ~ 1.1
-50	0.25 ~ 0.30	1.7 ~ 2.0
-60	0.71 ~ 0.88	4.7 ~ 5.8
-70	2.20 ~ 2.75	14.5 ~ 18.1
-80	6.95 ~ 8.69	45.8 ~ 57.3

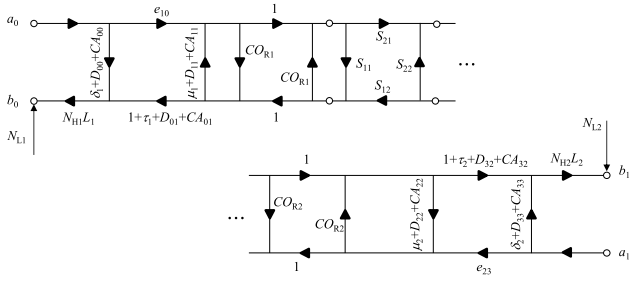

Fig. 16. Residual model including random effects of VNA.

measure the one-port S-parameter of a D-band power sensor shown in Fig. 18. The red and blue lines are measured at the KRISS and the PTB, respectively, and the shadow regions indicate the uncertainty of the level of confidence of 95%

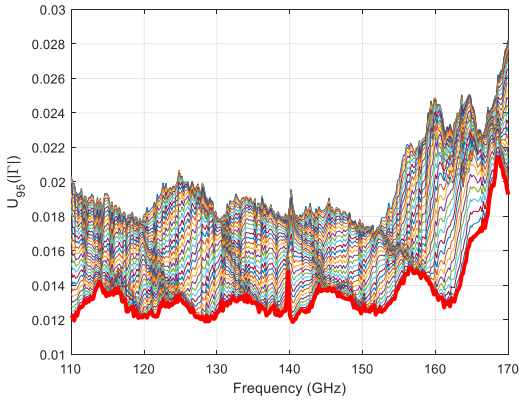

Fig. 17. Measurement uncertainty evaluated by the residual model where $|\Gamma| = 1.0$. The lines indicate the difference in values caused by different phase values. The thick lines indicate the smallest value.

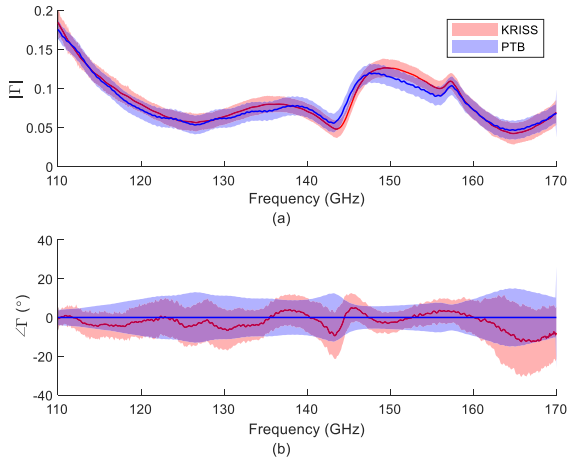

Fig. 18. Comparison of the reflection coefficient of a low reflective device, a power sensor. The lines denote measured values and shadow regions indicate a level of confidence of 95% ($k = 2$). The phases were normalized by the measured value of the PTB. (a) Magnitude. (b) Phase.

($k = 2$). The phase value has been normalized with the value measured by the PTB for easy comparison. We confirm that the two NMIs' measurement results agree with less than 1 of E_n for both magnitude and phase. Table IV shows the uncertainty budget for the magnitude of the compared DUT at 140 MHz detailed in Appendix. The largest uncertainty source is the residual uncertainty calculated in Section III. Especially, the imaginary of directivity is the primary uncertainty source. Note that the uncertainty contribution of each source depends on the DUT's reflection.

VIII. CONCLUSION

In this study, we establish and present an impedance standard for D-band. Shims, a flush short, thru, and a reciprocal device are used as the calibration standards. The shims are modeled with measured dimensions. By using the closed-form formula for shim modeling, calculation time is significantly reduced. We then model other calibration standards and use the eight-term VNA error model for our measurement system. We employ nonlinear optimization to obtain the error coefficients of the VNA error model. We evaluate the measurement uncertainty, including the uncertainty in the dimensional

TABLE IV
UNCERTAINTY BUDGET FOR THE MAGNITUDE OF THE LOW REFLECTIVE DEVICE AT 140 GHz

Quantity	Expected value	Standard uncertainty	Sensitivity coefficient	Uncertainty contribution
$\Re(\delta)$	0	0.00335	0.03852	0.00013
$\Im(\delta)$	0	0.00313	0.99926	0.00313
$\Re(\mu)$	0	0.00327	0.00000	0.00000
$\Im(\mu)$	0	0.00319	-0.00011	0.00000
$\Re(\tau)$	0	0.00615	0.01042	0.00006
$\Im(\tau)$	0	0.00663	0.00000	0.00000
$\Re(D_{00})$	0	0.00034	0.03850	0.00001
$\Im(D_{00})$	0	0.00083	0.99926	0.00083
$\Re(D_{11})$	0	0.00060	0.00000	0.00000
$\Im(D_{11})$	0	0.00360	-0.00011	0.00000
$\Re(D_{01})$	0	0.00098	0.01042	0.00001
$\Im(D_{01})$	0	0.00352	0.00000	0.00000
$\Re(CA_{00})$	0	0.00066	0.03852	0.00003
$\Im(CA_{00})$	0	0.00032	0.99926	0.00032
$\Re(CA_{11})$	0	0.00034	0.00000	0.00000
$\Im(CA_{11})$	0	0.00278	-0.00011	0.00000
$\Re(CA_{01})$	0	0.00123	0.01042	0.00001
$\Im(CA_{01})$	0	0.00252	0.00000	0.00000
$\Re(CO_{\mathrm{R}})$	0	0.00005	0.03851	0.00000
$\Im(CO_{\mathrm{R}})$	0	0.00167	0.99915	0.00167
$\lvert L\rvert$	1	0.00180	0.01042	0.00002
$\angle L$	0	0.00180	0.00000	0.00000
$\Re(N_{\mathrm{L}})$	0	0.00005	0.03850	0.00000
$\Im(N_{\mathrm{L}})$	0	0.00005	0.99926	0.00004
$\lvert N_{\mathrm{H}}\rvert$	1	0.00010	0.01042	0.00000
$\angle N_{\mathrm{H}}$	0	0.01000	0.00000	0.00000
Combined standard uncertainty ($k = 1$)				0.00366

measurement of the calibration standards, the fitting uncertainty of the optimization, and VNA random effects. We also propose a novel method to evaluate the drift, nonlinearity, and test port cable stability for the random effects of the VNA. The results show, for reflection of 0–1.0, the expanded uncertainty ($k = 2$) is 0.006–0.021, and 0.8°–6.2° for magnitude and phase, respectively. For transmission of −80 to 0 dB, the expanded uncertainty is 8.69–0.10 dB and 57.3°–0.7° for magnitude and phase, respectively. In the future, we plan to promote bilateral comparisons between NMIs where CMC is registered. Also, we expect the present method can provide an efficient approach that can be used to establish impedance standards in other sub-THz candidate frequency bands.

APPENDIX

This appendix describes the evaluation of uncertainty contributions given in the uncertainty budget of Table IV. Each uncertainty is easily calculated product of the Jacobian matrix and covariance matrix similar to (23). For example, if we consider the noise floor of the VNA, we should propagate the covariance of the noise floor to the S-parameters of the DUT

$$\Sigma_{N_{L1}}^{\mathrm{DUT}} = J_{N_{L1}} \Sigma_{N_{L1}} J'_{N_{L1}} \tag{A1}$$

where $\Sigma_{N_{L1}}$ is the covariance for the noise floor, and $J_{N_{L1}}$ Jacobian matrix. If there is no correlation between cross-frequency components, the covariance of the noise floor $\Sigma_{N_{L1}}$ is composed of a 2-by-2 matrix as follows:

$$\Sigma_{N_{L1}} = \begin{bmatrix} \sigma^2_{\Re(N_{L1})} & \sigma_{\Re(N_{L1})}\sigma_{\Im(N_{L1})} \\ \sigma_{\Im(N_{L1})}\sigma_{\Re(N_{L1})} & \sigma^2_{\Im(N_{L1})} \end{bmatrix} \tag{A2}$$

where σ represents the limitation obtained in Fig. 9, and $\sigma_{\Re(N_{L1})} = \sigma_{\Im(N_{L1})}$. The Jacobian matrix in (A1) is given by

$$J_{N_{L1}} = \begin{bmatrix} \frac{\partial \Re(S_{11,m})}{\partial \Re(N_{L1})} & \frac{\partial \Re(S_{11,m})}{\partial \Im(N_{L1})} \\ \frac{\partial \Im(S_{11,m})}{\partial \Re(N_{L1})} & \frac{\partial \Im(S_{11,m})}{\partial \Im(N_{L1})} \\ \vdots & \vdots \\ \frac{\partial \Im(S_{22,m})}{\partial \Re(N_{L1})} & \frac{\partial \Im(S_{22,m})}{\partial \Im(N_{L1})} \end{bmatrix} = \begin{bmatrix} 1 & 0 \\ 0 & 1 \\ 0 & 0 \\ 0 & 0 \\ 1 & 0 \\ 0 & 1 \\ 0 & 0 \\ 0 & 0 \end{bmatrix} \tag{A3}$$

which can be easily calculated by numerical partial differentiation of

$$\begin{aligned} &\begin{bmatrix} S_{11,m} & S_{12,m} \\ S_{21,m} & S_{22,m} \end{bmatrix} \\ &= \left(\begin{bmatrix} \delta_1 + D_{00} + CA_{00} & 1 + \tau_1 + D_{01} + CA_{01} \\ 1 & \mu_1 + D_{11} + CA_{11} \end{bmatrix} \right. \\ &\quad \oplus \begin{bmatrix} CO_{R1} & 1 \\ 1 & CO_{R1} \end{bmatrix} \oplus \begin{bmatrix} S_{11} & S_{12} \\ S_{21} & S_{22} \end{bmatrix} \\ &\quad \oplus \begin{bmatrix} CO_{R2} & 1 \\ 1 & CO_{R2} \end{bmatrix} \\ &\quad \left. \oplus \begin{bmatrix} \mu_2 + D_{22} + CA_{22} & 1 \\ 1 + \tau_2 + D_{32} + CA_{32} & \delta_2 + D_{22} + CA_{22} \end{bmatrix} \right) \\ &\quad \circ \begin{bmatrix} N_{H1}L_1 & N_{H1}L_1 \\ N_{H2}L_2 & N_{H2}L_2 \end{bmatrix} + \begin{bmatrix} N_{L1} & N_{L1} \\ N_{L2} & N_{L2} \end{bmatrix} \end{aligned} \tag{A4}$$

where the symbol "∘" denotes an element-wise product.

In (A4), $S_{11,m} = b_0/a_0$, $S_{12,m} = b_0/a_1$, $S_{21,m} = b_1/a_0$, and $S_{22,m} = b_1/a_1$. Note that in numerical partial differentiation, $S_{ij,m}$ was made into a one-column dimensional array as $[\Re(S_{11,m})\Im(S_{11,m})\Re(S_{21,m}), \ldots, \Im(S_{22,m})]$.

The total covariance of the S-parameters of the DUT is a summation of each covariance such as the residual uncertainty, the noise floor, the trace noise, the nonlinearity, the drift, the test port cable stability, and the connection repeatability. Finally, the expanded uncertainty is obtained by taking the square root of the diagonal matrix of the total covariance and multiplying the appropriate coverage factor k.

ACKNOWLEDGMENT

The authors are very grateful to Dr. Karsten Kuhlmann and Mr. Florian Rausche of the PTB, Germany for their help and comments in comparing the reflection coefficient of the *D*-band power sensor.

REFERENCES

[1] M. Z. Chowdhury, M. Shahjalal, S. Ahmed, and Y. M. Jang, "6G wireless communication systems: Applications, requirements, technologies, challenges, and research directions," *IEEE Open J. Commun. Soc.*, vol. 1, pp. 957–975, 2020, doi: 10.1109/OJCOMS.2020.3010270.

[2] I. F. Akyildiz, A. Kak, and S. Nie, "6G and beyond: The future of wireless communications systems," *IEEE Access*, vol. 8, pp. 133995–134030, 2020, doi: 10.1109/ACCESS.2020.3010896.

[3] Samsung Research. *6G Spectrum: Expanding the Frontier*. Accessed: Jul. 11, 2023. [Online]. Available: https://d110erj175o600.cloudfront.net/wp-content/uploads/2022/05/11124401/2022May_6G_Spectrum.pdf

[4] M. Horibe and R. Kishikawa, "Metrological traceability in waveguide S-parameter measurements at 1.0 THz band," *IEEE Trans. Instrum. Meas.*, vol. 62, no. 6, pp. 1814–1820, Jun. 2013, doi: 10.1109/TIM.2013.2240953.

[5] N. M. Ridler and R. G. Clarke, "Establishing traceability to the international system of units for scattering parameter measurements from 750 GHz to 1.1 THz," *IEEE Trans. Terahertz Sci. Technol.*, vol. 6, no. 1, pp. 2–11, Jan. 2016, doi: 10.1109/TTHZ.2015.2502068.

[6] M. Horibe, "Measurement uncertainty model for vector network analyzers with frequency extension modules at terahertz frequencies," *IEEE Trans. Instrum. Meas.*, vol. 66, no. 6, pp. 1605–1612, Jun. 2017, doi: 10.1109/TIM.2017.2668718.

[7] N. M. Ridler, R. G. Clarke, C. Li, and M. J. Salter, "Strategies for traceable submillimeter-wave vector network analyzer," *IEEE Trans. Terahertz Sci. Technol.*, vol. 9, no. 4, pp. 392–398, Jul. 2019, doi: 10.1109/TTHZ.2019.2911870.

[8] N. M. Ridler, S. Johny, X. Shang, W. Sun, and A. Wilson, "Comparing standardized and manufacturers' interfaces for waveguides used at submillimeter wavelengths," *IEEE Trans. Terahertz Sci. Technol.*, vol. 10, no. 5, pp. 453–459, Sep. 2020, doi: 10.1109/TTHZ.2020.3010122.

[9] N. M. Ridler, S. Johny, M. J. Salter, X. Shang, W. Sun, and A. Wilson, "Establishing waveguide lines as primary standards for scattering parameter measurements at submillimetre wavelengths," *Metrologia*, vol. 58, no. 1, Jan. 2021, Art. no. 015015, doi: 10.1088/1681-7575/abd371.

[10] C. Cho, T.-W. Kang, J.-Y. Kwon, and H. Koo, "Establishment of D-band waveguide impedance standard for 6G wireless communications," in *CPEM Dig.*, Wellington, New Zealand, Dec. 2022, pp. 1–2.

[11] T.-W. Kang, C. Cho, J.-Y. Kwon, and H. Koo, "Evaluation of vector network analyzer with D-band frequency extenders using motorized waveguide switches," in *CPEM Dig.*, Wellington, New Zealand, Dec. 2022, pp. 1–2.

[12] D. F. Williams, J. C. M. Wang, and U. Arz, "An optimal vector-network-analyzer calibration algorithm," *IEEE Trans. Microw. Theory Techn.*, vol. 51, no. 12, pp. 2391–2401, Dec. 2003, doi: 10.1109/TMTT.2003.819211.

[13] D. Kent Rytting, "Network analyzer accuracy overview," in *Proc. 58th ARFTG Conf. Dig.*, vol. 40, Nov. 2001, pp. 1–13, doi: 10.1109/ARFTG.2001.327486.

[14] (2018). *Guidelines on Evaluation of Vector Network Analyzers (Calibration Guide no. 12, Version 3.0)*. [Online]. Available: https://www.euramet.org/publications-media-centre/calibration-guidelines

[15] M. Zeier, J. Hoffmann, P. Hürlimann, J. Rüfenacht, D. Stalder, and M. Wollensack, "Establishing traceability for the measurement of scattering parameters in coaxial line systems," *Metrologia*, vol. 55, no. 1, pp. S23–S36, Feb. 2018, doi: 10.1088/1681-7575/aaa21c.

[16] D. F. Williams, "500 GHz–750 GHz rectangular-waveguide vector-network-analyzer calibrations," *IEEE Trans. Terahertz Sci. Technol.*, vol. 1, no. 2, pp. 364–377, Nov. 2011, doi: 10.1109/TTHZ.2011.2127370.

[17] R. B. Marks, "Formulations of the basic vector network analyzer error model including switch-terms," in *Proc. 50th ARFTG Conf. Dig.*, vol. 32, Dec. 1997, pp. 115–126, doi: 10.1109/ARFTG.1997.327265.

[18] J. A. Jargon, D. F. Williams, and A. Sanders, "The relationship between switch-term-corrected scattering-parameters and wave-parameters measured with a two-port vector network analyzer," *IEEE Microw. Wireless Compon. Lett.*, vol. 28, no. 10, pp. 951–953, Oct. 2018, doi: 10.1109/LMWC.2018.2867076.

[19] G. R. Simpson, "A generalized n-port cascade connection," in *IEEE MTT-S Int. Microw. Symp. Dig.*, Jun. 1981, pp. 507–509, doi: 10.1109/MWSYM.1981.1129978.

[20] D. F. Williams, "Comparison of sub-millimeter-wave scattering-parameter calibrations with imperfect electrical ports," *IEEE Trans. Terahertz Sci. Technol.*, vol. 2, no. 1, pp. 144–152, Jan. 2012, doi: 10.1109/TTHZ.2011.2167833.

[21] M. Horibe, R. Kishikawa, and M. Shida, "Complete characterization of rectangular waveguide measurement standards for vector network analyzer in the range of millimeter and sub-millimeter wave frequencies," in *Proc. 76th ARFTG Microw. Meas. Conf.*, Nov. 2010, pp. 1–15, doi: 10.1109/ARFTG76.2010.5700053.

[22] J. A. Jargon, "Physical models and dimensional traceability of WR15 rectangular waveguide standards for determining systematic uncertainties of calibrated scattering parameters," Nat. Inst. Standards Technol. (NIST), Gaithersburg, MD, USA, NIST Tech. Note 2109, Aug. 2020.

[23] R. B. Marks, "A multiline method of network analyzer calibration," *IEEE Trans. Microw. Theory Techn.*, vol. 39, no. 7, pp. 1205–1215, Jul. 1991, doi: 10.1109/22.85388.

[24] J. Hoffmann, D. Stalder, M. Wollensack, J. Ruefenacht, and M. Zeier, "Considerations for using waveguide extenders," in *Proc. Conf. Precis. Electromagn. Meas. (CPEM)*, Jul. 2016, pp. 1–2, doi: 10.1109/CPEM.2016.7540505.

[25] J. Hoffmann, D. Stalder, M. Wollensack, J. Ruefenacht, and M. Zeier, "Temperature control of waveguide extenders," in *Proc. Conf. Precis. Electromagn. Meas. (CPEM)*, Jul. 2016, pp. 1–2, doi: 10.1109/CPEM.2016.7540615.

[26] *Oshima Prototype Engineering, UG Clamp*. Accessed: Jul. 11, 2023. [Online]. Available: https://oshimashisaku.jp/English/e-m-Wave/wg_UGc.php

[27] C. Cho, J.-G. Lee, T.-W. Kang, and N.-W. Kang, "Calibration and uncertainty analysis of sample-time error on high jitter of samplers," *J. Electromagn. Eng. Sci.*, vol. 18, no. 3, pp. 169–174, Jul. 2018, doi: 10.26866/jees.2018.18.3.169.

[28] D. F. Williams. *NIST Microwave Uncertainty Framework*. [Online]. Available: https://www.nist.gov/services-resources/software/wafer-calibration-software accessed May 30, 2022).

[29] C. Cho, T. Kang, J. Kwon, and H. Koo, "A novel method for estimating residual model parameters to evaluate uncertainty in scattering parameter measurements," *IEEE Trans. Instrum. Meas.*, vol. 71, pp. 1–8, 2022, doi: 10.1109/TIM.2022.3208645.

[30] C. Cho, J. Kwon, H. Koo, and T. Kang, "Uncertainty analysis of scattering parameters calibrated by an electronic calibration unit based on a residual model," *IEEE Access*, vol. 10, pp. 6328–6337, 2022, doi: 10.1109/ACCESS.2022.3141310.

[31] A. C. Stelson, A. M. Hagerstrom, J. A. Jargon, and C. J. Long, "Quantifying receiver nonlinearities in VNA measurements for the WR-15 waveguide band," *IEEE Trans. Microw. Theory Techn.*, vol. 70, no. 5, pp. 2743–2749, May 2022, doi: 10.1109/TMTT.2022.3155466.

Chihyun Cho (Senior Member, IEEE) received the B.S., M.S., and Ph.D. degrees in electronic and electrical engineering from Hongik University, Seoul, South Korea, in 2004, 2006, and 2009, respectively.

From 2009 to 2012, he participated in the development of military communication systems at the Communication Research and Development Center, Samsung Thales, Bundang-gu, Seongnam, South Korea. Since 2012, he has been with the Korea Research Institute of Standards and Science (KRISS), Daejeon, South Korea. In 2014, he was a Guest Researcher at the National Institute of Standards and Technology (NIST), Boulder, CO, USA. He also served on the Presidential Advisory Council on Science and Technology (PACST), Seoul, from 2016 to 2017. His current research interests include microwave metrology, time-domain measurement, and standard of communication parameters.

Tae-Weon Kang (Senior Member, IEEE) received the B.S. degree in electronic engineering from Kyungpook National University, Daegu, South Korea, in 1988, and the M.S. and Ph.D. degrees in electronic and electrical engineering from the Pohang University of Science and Technology (POSTECH), Pohang, South Korea, in 1990 and 2001, respectively.

Since 1990, he has been with the Center for Electromagnetic Metrology, Division of Physical Metrology, Korea Research Institute of Standards and Science, Daejeon, South Korea, working on electromagnetic metrology, and he is there as a Principal Research Scientist. In 2002, he has spent a year as a Visiting Researcher under the Korea Science and Engineering Foundation Post-Doctoral Fellowship Program at the George Green Institute for Electromagnetics Research, University of Nottingham, Nottingham, U.K., and he worked there on measurement of absorbing performance of electromagnetic absorbers and on a generalized transmission line modeling method. His research interests include electromagnetic metrology such as electromagnetic power, noise, RF voltage, impedance, and antenna characteristics, and numerical modeling in electromagnetic compatibility.

Dr. Kang received the outstanding researcher award from the Korean Institute of Electromagnetic Engineering and Science (KIEES) in 2017. Since 2018, he has served as an Associate Editor of the IEEE TRANSACTIONS ON INSTRUMENTATION AND MEASUREMENT.

Jae-Yong Kwon (Senior Member, IEEE) received the B.S. degree in electronics from Kyungpook National University, Daegu, South Korea, in 1995, and the M.S. and Ph.D. degrees in electrical engineering from the Korea Advanced Institute of Science and Technology, Daejeon, South Korea, in 1998 and 2002, respectively.

He was a Visiting Scientist with the Department of High-Frequency and Semiconductor System Technologies, Technical University of Berlin, Berlin, Germany, with the National Institute of Standards and Technology (NIST), Boulder, CO, USA, and also with PTB, Brunswick, Germany, in 2001, 2010, and 2019, respectively. From 2002 to 2005, he was a Senior Research Engineer with the Devices and Materials Laboratory, LG Electronics Institute of Technology, Seoul, South Korea. Since 2005, he has been with the Korea Research Institute of Standards and Science, Daejeon, where he is currently the Head of the Electromagnetic Wave Metrology Group and a Principal Research Scientist. Since 2013, he has been a Professor of Science of Measurement with the University of Science and Technology, Daejeon. His current research interests include electromagnetic power, impedance, and antenna measurement.

Dr. Kwon is a Korea Institute of Electromagnetic Engineering and Science (KIEES) Life Member and an IEICE Member.

Hyunji Koo (Member, IEEE) received the B.S. and Ph.D. degrees in electrical engineering from the Korea Advanced Institute of Science and Technology (KAIST), Daejeon, South Korea, in 2008 and 2015, respectively.

From March to August 2015, she was a Post-Doctoral Research Fellow at the School of Electrical Engineering, KAIST. Since September 2015, she has been a Senior Research Scientist of the Electromagnetic Wave Metrology Group, Korea Research Institute of Standards and Science (KRISS), Daejeon. In 2018, she was a Visiting Researcher at the National Physical Laboratory (NPL), Teddington, U.K. Her current research interests include the characterization of on-wafer devices.